# Supplementary Information

Alignment of methylcellulose nanofibrils through confinement

Aref Ghaemi, Maryam Roza Yazdani McCord, Tero Mäkinen, Juha Koivisto and Mikko Alava

Department of Applied Physics, Aalto University, Espoo, Finland

This document supports the main text in three parts. Section S1 gives the full derivation of the confinement model, its numerical solution and verification, and the estimation of its parameters, including their sensitivity, uncertainty and residuals. Section S2 describes freeze-dried MC foams, in which nanofibril alignment was also observed. Section S3 describes the measurement of fibril lengths from SEM images used to test the fitted fibril length.

## S1 Confinement model

### S1.1 Derivation

Fibrils are represented as rigid, monodisperse rods of length $L$ and diameter $D$ confined between two flat, parallel walls a distance $H$ apart. The model makes three approximations: interactions between rods are treated at the level of the second virial coefficient (Onsager-type mean field); the walls act only as hard boundaries; and the tilt distribution is set by the confinement geometry alone, so that interactions act only on the in-plane orientation.

#### S1.1.1 Orientations

The orientation of a rod is described by its azimuthal angle $\varphi$ in the film plane and its tilt angle $\beta$ measured from the film plane,

$$\mathbf{u}(\varphi, \beta) = (\cos\beta\cos\varphi,\ \cos\beta\sin\varphi,\ \sin\beta). \tag{S1}$$

Because the rods are apolar ($\mathbf{u}$ and $-\mathbf{u}$ are equivalent), it suffices to take $\varphi \in [0, \pi)$ and $\beta \in [-\pi/2, \pi/2]$. With $\beta$ measured from the plane rather than from the normal, the element of solid angle is

$$\mathrm{d}\Omega = \cos\beta\ \mathrm{d}\beta\,\mathrm{d}\varphi. \tag{S2}$$

#### S1.1.2 Tilt distribution under confinement

A rod tilted by $\beta$ spans a vertical extent $L|\sin\beta| + D$, so it fits between the walls only if

$$L\,|\sin\beta| + D \le H. \tag{S3}$$

The largest accessible tilt is therefore

$$\beta_{\max}(H) = \sin^{-1}\left[\min\left(1, \frac{H-D}{L}\right)\right]. \tag{S4}$$

For a given tilt, the centre of the rod can be placed anywhere within a vertical range of width

$$a_H(\beta) = \left[H - D - L\,|\sin\beta|\right]_+, \tag{S5}$$

where $[x]_+ = \max(x, 0)$. In the absence of interactions, the probability of a tilt is proportional to its share of orientational phase space, Eq. (S2), times the translational room it leaves, Eq. (S5). The normalised tilt distribution is therefore

$$q_H(\beta) = \frac{\cos\beta\ [H - D - L\,|\sin\beta|]_+}{Z_\beta(H)}, \tag{S6}$$

with

$$Z_\beta(H) = \int_{-\pi/2}^{\pi/2} \cos\beta\ [H - D - L\,|\sin\beta|]_+ \,\mathrm{d}\beta. \tag{S7}$$

For $H \gg L$, the room $a_H(\beta) \approx H - D$ is nearly independent of $\beta$, and $q_H(\beta) \propto \cos\beta$, which corresponds to isotropic orientations in three dimensions. As $H \to D$, $\beta_{\max} \to 0$ and the rods are confined to the film plane. Decreasing $H$ thus continuously restricts the rods towards $\beta = 0$.

### S1.1.3 Interaction kernels and tilt averaging

The angle $\gamma$ between two rods with orientations $(\varphi, \beta)$ and $(\varphi', \beta')$ follows from $\cos\gamma = \mathbf{u} \cdot \mathbf{u}'$,

$$\cos\gamma = \cos\beta\cos\beta'\cos(\varphi - \varphi') + \sin\beta\sin\beta'. \tag{S8}$$

Two angular interaction kernels of the form $K_p = |\sin\gamma|^p$ are considered,

$$K_1(\gamma) = |\sin\gamma|, \qquad K_2(\gamma) = \sin^2\gamma. \tag{S9}$$

The $p = 1$ kernel is the angular dependence of the excluded volume of two slender hard rods (Onsager 1949). The $p = 2$ kernel is a smoother, quadratic alternative, used to test how far the conclusions depend on the assumed interaction law. SEM resolves only the projected, in-plane orientation of the fibrils, so the kernel is averaged over the tilts of both rods,

$$\bar{K}_p(\Delta\varphi; H, L, D) = \iint q_H(\beta)\, q_H(\beta')\, K_p(\gamma(\Delta\varphi, \beta, \beta'))\,\mathrm{d}\beta\,\mathrm{d}\beta', \tag{S10}$$

with $\Delta\varphi = \varphi - \varphi'$. When both rods lie flat, $\gamma = \Delta\varphi$, and the kernel penalises in-plane misalignment as strongly as possible; tilts make $\gamma$ less sensitive to $\Delta\varphi$ and so dilute the penalty. Film thickness thus enters the in-plane problem only through $\bar{K}_p$.

### S1.1.4 Free energy and self-consistent distribution

The joint orientational distribution is approximated as

$$\Psi_H(\varphi, \beta) = f_H(\varphi)\, q_H(\beta), \tag{S11}$$

where $q_H(\beta)$ is fixed by the confinement geometry and $f_H(\varphi)$ is the in-plane distribution to be determined. The dimensionless orientational free energy is

$$F_p[f; H] = \int_0^\pi f(\varphi)\ln f(\varphi)\,\mathrm{d}\varphi + \frac{c_\infty}{2}\int_0^\pi\!\!\int_0^\pi f(\varphi)\, f(\varphi')\, \bar{K}_p(\varphi - \varphi'; H)\,\mathrm{d}\varphi\,\mathrm{d}\varphi', \tag{S12}$$

subject to

$$\int_0^\pi f_H(\varphi)\,\mathrm{d}\varphi = 1. \tag{S13}$$

The first term is the orientational entropy and the second the excluded-volume interaction. The parameter $c_\infty$ sets the strength of the interaction relative to the entropy. In Onsager theory it would be proportional to the number density times the rod dimensions; here it is treated as an independent effective parameter, so that $L$ enters the model only through the tilt distribution. Requiring $F_p$ to be stationary under variations of $f$ that preserve Eq. (S13) gives

$$f_H(\varphi) = \frac{1}{Z_H}\exp\!\left[-c_\infty \int_0^\pi f_H(\varphi')\, \bar{K}_p(\varphi - \varphi'; H)\,\mathrm{d}\varphi'\right], \tag{S14}$$

with $Z_H$ fixed by Eq. (S13).

### S1.1.5 Isotropic solution and onset of order

Because $\bar{K}_p$ depends only on $\Delta\varphi$, the isotropic distribution

$$f_{\mathrm{iso}}(\varphi) = \frac{1}{\pi}, \qquad S_{\mathrm{iso}} = 0, \tag{S15}$$

always solves Eq. (S14). Its stability follows from the Fourier series of the averaged kernel,

$$\bar{K}_p(\Delta\varphi; H) = k_0(H) + \sum_{n\geq 1} k_n(H)\cos(2n\Delta\varphi). \tag{S16}$$

Inserting $f = 1/\pi + \varepsilon\cos 2\varphi$ into Eq. (S14) and linearising in $\varepsilon$, using $\int_0^\pi \cos 2\varphi' \cos 2(\varphi-\varphi')\,\mathrm{d}\varphi' = (\pi/2)\cos 2\varphi$, gives a non-trivial solution when

$$c_\infty\,|k_1(H)| = 2, \tag{S17}$$

where $k_1 < 0$ for both kernels. The isotropic state is unstable towards in-plane order when $c_\infty|k_1(H)| > 2$. For rods lying flat, $|\sin\Delta\varphi|$ has $k_1 = -4/(3\pi)$ and $\sin^2\Delta\varphi$ has $k_1 = -1/2$, so ordering requires $c_\infty > 3\pi/2 \approx 4.71$ for $p = 1$ and $c_\infty > 4$ for $p = 2$. Tilting reduces $|k_1(H)|$, so for $c_\infty$ above these values the films order below a crossover thickness $H^*$ defined by $c_\infty|k_1(H^*)| = 2$. The fitted values ($c_\infty = 5.98$ for $p = 1$ and 5.38 for $p = 2$) lie above the respective flat-rod thresholds, as required for the thinnest films to be ordered, and the crossover thicknesses of the local model are $H^* = 779$ nm ($p = 1$) and 743 nm ($p = 2$) (Sec. S1.2.3). Evaluating Eq. (S17) with the averaged kernel gives $H^* = 778$ nm for $p = 1$ and 745 nm for $p = 2$, within 2 nm of the transitions found by branch tracking, confirming that the numerical solution and the analytic onset criterion agree.

### S1.1.6 Order parameter

The predicted in-plane order parameter is

$$S(H) = \left|\langle e^{2i\varphi}\rangle\right| = \sqrt{\langle\cos 2\varphi\rangle^2 + \langle\sin 2\varphi\rangle^2}, \tag{S18}$$

with averages over $f_H(\varphi)$, the same quantity as the measured order parameter (main text, Eq. 1). Film thickness enters only through the accessible tilts,

$$H \;\to\; q_H(\beta) \;\to\; \bar{K}_p \;\to\; f_H(\varphi) \;\to\; S(H), \tag{S19}$$

so the thickness dependence of $S$ is not prescribed but follows from the confinement geometry.

### S1.1.7 Local thickness variation

The observable order parameter is modeled as an average of the local prediction $S_0(h)$ over a distribution of local thicknesses $h$,

$$S_{\mathrm{obs}}(H) = \int S_0(h; c_\infty, L, D, p)\, P(h \mid H, \sigma_H)\,\mathrm{d}h, \tag{S20}$$

with a truncated, renormalised Gaussian

$$P(h \mid H, \sigma_H) \propto \exp\left[-\frac{(h-H)^2}{2\sigma_H^2}\right]. \tag{S21}$$

This averaging leaves the local physics unchanged and serves as an observation model linking the local prediction to the spatially averaged measurement. Its effect is quantified in Sec. S1.2.4.

## S1.2 Numerical solution and verification

### S1.2.1 Implementation

Equation (S14) was solved on a uniform product grid in $\varphi$ and $\beta$ by damped fixed-point iteration, with $q_H(\beta)$ evaluated analytically at each node. Unless stated otherwise, all results use $n_\varphi = 72$ azimuthal and $n_\beta = 61$ tilt nodes, a fixed-point tolerance of $10^{-8}$ and a mixing parameter of 0.06.

### S1.2.2 Grid convergence

To confirm that the computed order parameter is insensitive to the angular discretisation, $S(H)$ was recomputed at the best-fit parameters on successively finer grids and compared with the finest grid ($n_\varphi = 120$, $n_\beta = 101$) as reference (Table S1, Fig. S1). The largest deviation anywhere in the tested range is $\max|\Delta S| = 5.4 \times 10^{-3}$, on the coarsest grid for the $p = 2$ kernel, and it decreases monotonically under refinement. The coefficient of determination varies by less than $3 \times 10^{-3}$ across all grids for either kernel. The production grid is therefore converged at the precision relevant to the fit.

**Table S1:** Grid convergence of the predicted order parameter at fixed best-fit parameters. Deviations are taken with respect to the finest grid, whose deviation is zero by construction.

| $p$ | $n_\varphi$ | $n_\beta$ | SSE | $R^2$ | $\max\|\Delta S\|$ | rms $\Delta S$ |
|---|---|---|---|---|---|---|
| 1 | 48 | 41 | 0.094668 | 0.824798 | $2.38 \times 10^{-3}$ | $1.02 \times 10^{-3}$ |
| 1 | 72 | 61 | 0.094681 | 0.824775 | $7.89 \times 10^{-4}$ | $3.34 \times 10^{-4}$ |
| 1 | 96 | 81 | 0.094686 | 0.824765 | $2.48 \times 10^{-4}$ | $1.05 \times 10^{-4}$ |
| 1 | 120 | 101 | 0.094689 | 0.824760 | – | – |
| 2 | 48 | 41 | 0.103263 | 0.808892 | $5.37 \times 10^{-3}$ | $1.75 \times 10^{-3}$ |
| 2 | 72 | 61 | 0.101837 | 0.811530 | $2.59 \times 10^{-4}$ | $1.57 \times 10^{-4}$ |
| 2 | 96 | 81 | 0.101867 | 0.811476 | $8.38 \times 10^{-5}$ | $5.07 \times 10^{-5}$ |
| 2 | 120 | 101 | 0.101881 | 0.811449 | – | – |

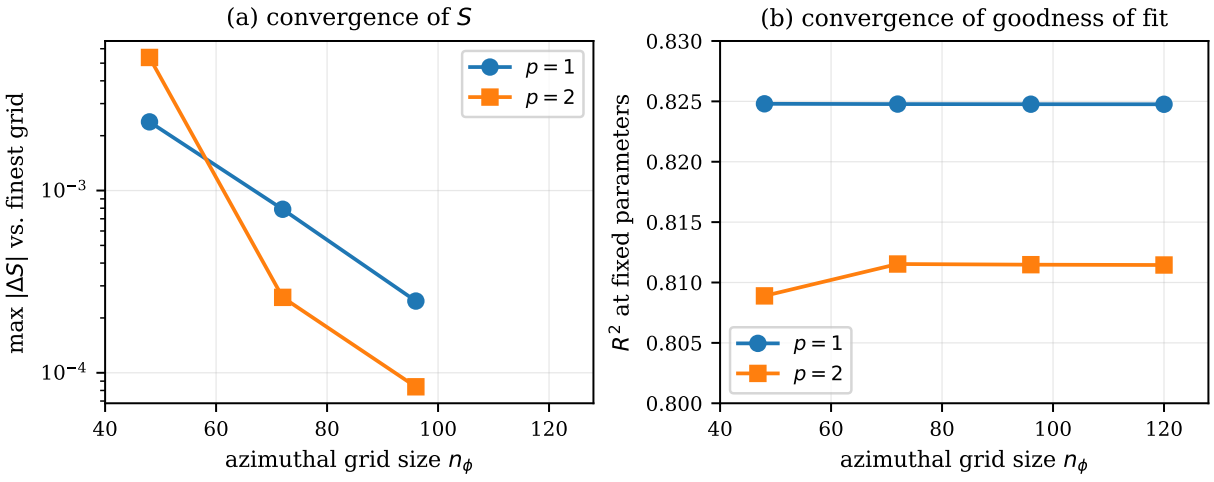


**Figure S1:** Convergence of the numerical solution with angular grid refinement. (a) Maximum absolute deviation of the predicted $S(H)$ from the finest-grid reference, on a logarithmic scale; the reference grid ($n_\varphi = 120$) is omitted since its deviation vanishes by construction. (b) Coefficient of determination at fixed best-fit parameters. Both kernels are converged to better than $10^{-3}$ in $S$ on the production grid.

### S1.2.3 Branch continuation and equilibrium selection

Because Eq. (S14) is non-linear, the isotropic solution, Eq. (S15), and an ordered solution with $S > 0$ can coexist. Started from a nearly isotropic guess, the iteration can converge to the isotropic solution even where an ordered one exists, which would cause a premature, numerical loss of order near the crossover. The ordered solution was therefore followed by branch continuation: starting from the most strongly confined film, the converged distribution at one thickness was used as the initial guess at the next. The equilibrium state was determined independently from the free-energy difference

$$\Delta F(H) = F_p[f_{\mathrm{ord}}; H] - F_p[f_{\mathrm{iso}}; H], \tag{S22}$$

evaluated with Eq. (S12); the ordered state is favoured for $\Delta F < 0$.

The continued branch and the equilibrium branch coincide to within machine precision across the full thickness range for both kernels: the largest discrepancy $\max_H |S_{\mathrm{ordered}} - S_{\mathrm{equilibrium}}|$ is numerically zero over all 700 sampled thicknesses (Fig. S2). For both kernels $\Delta F$ is negative at small $H$ ($-0.076$ for $p = 1$ and $-0.085$ for $p = 2$ at $H = 15$ nm), increases smoothly and monotonically with thickness, and approaches zero continuously at the transition ($\Delta F = -3.2 \times 10^{-8}$ at $H = 779$ nm for $p = 1$, and $-3.2 \times 10^{-7}$ at $H = 743$ nm for $p = 2$; Fig. S3). No discontinuity or crossing occurs. Beyond these thicknesses the ordered solution ceases to exist and only the isotropic state remains. The loss of order at large $H$ is therefore a continuous equilibrium prediction of the model, consistent with the onset criterion of Eq. (S17), and not a numerical switch to the isotropic branch.

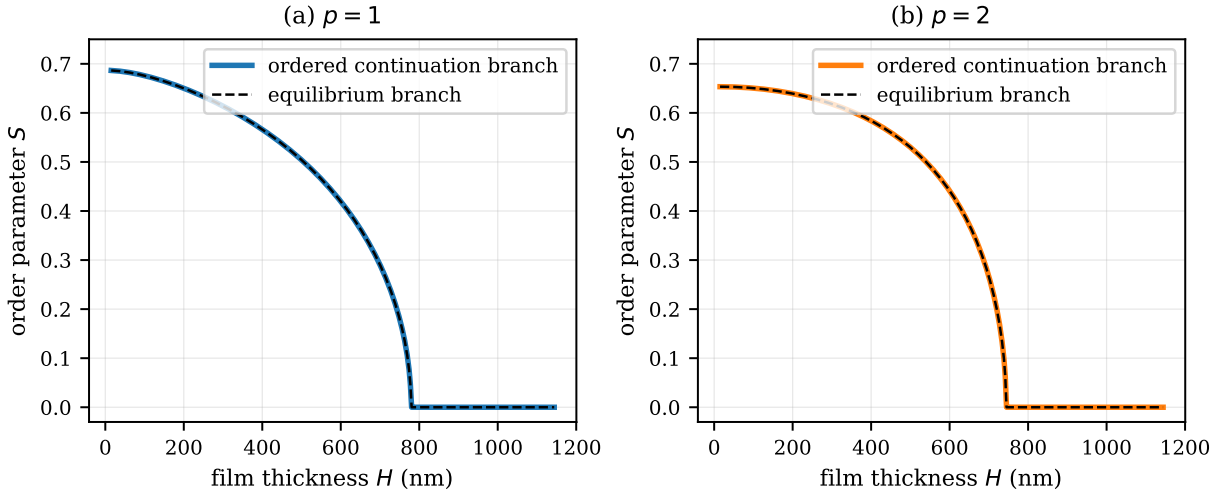


**Figure S2:** Ordered continuation branch (colored) compared with the branch selected by minimizing the free energy (dashed black), for the (a) $p = 1$ and (b) $p = 2$ kernels. The curves are indistinguishable, confirming that the continuation tracks the thermodynamically selected state rather than an arbitrary local solution.

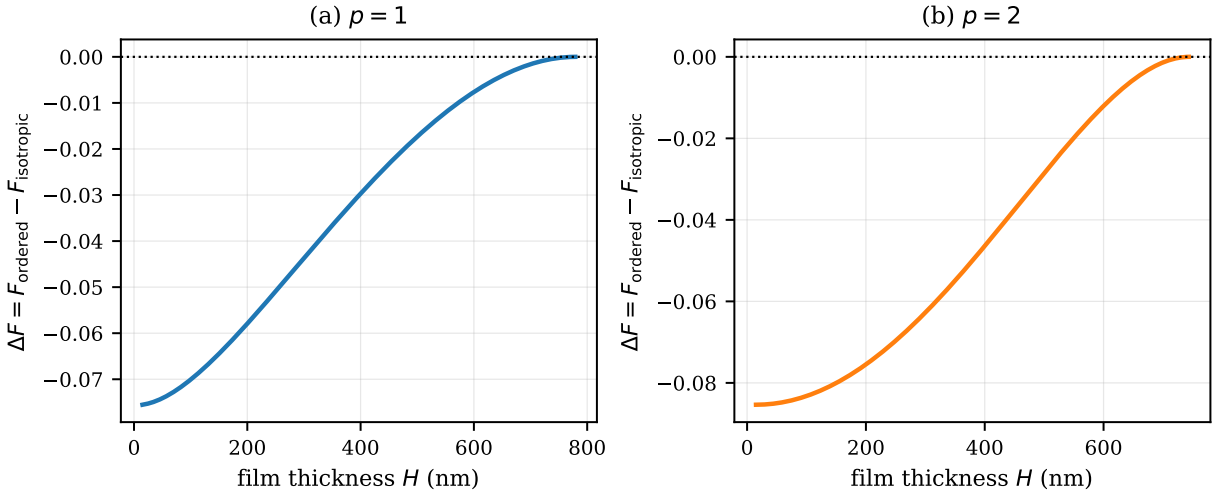


**Figure S3:** Free-energy difference $\Delta F = F_{\text{ordered}} - F_{\text{isotropic}}$ as a function of film thickness for the (a) $p = 1$ and (b) $p = 2$ kernels. $\Delta F$ rises smoothly to zero at the orientational transition; beyond it the ordered solution no longer exists and the curve terminates.

### S1.2.4 Effect of thickness averaging

Figure S4 compares the local model $S_0(h)$ with the thickness-averaged observable $S_{\text{obs}}(H)$, Eq. (S20). The two agree closely away from the transition, differing on average by only 0.008 ($p = 1$) and 0.010 ($p = 2$) across the plotted range. The averaging acts almost exclusively near the transition, where it replaces the abrupt cutoff of the local model by a gradual crossover; the largest differences are 0.092 at $H \approx 780$ nm for $p = 1$ and 0.111 at $H \approx 745$ nm for $p = 2$. This is the expected behaviour of an observation model: regions of a foam wall that are locally thinner than the nominal thickness can remain ordered while thicker regions have already become isotropic, smoothing the measured transition without altering the local physics.

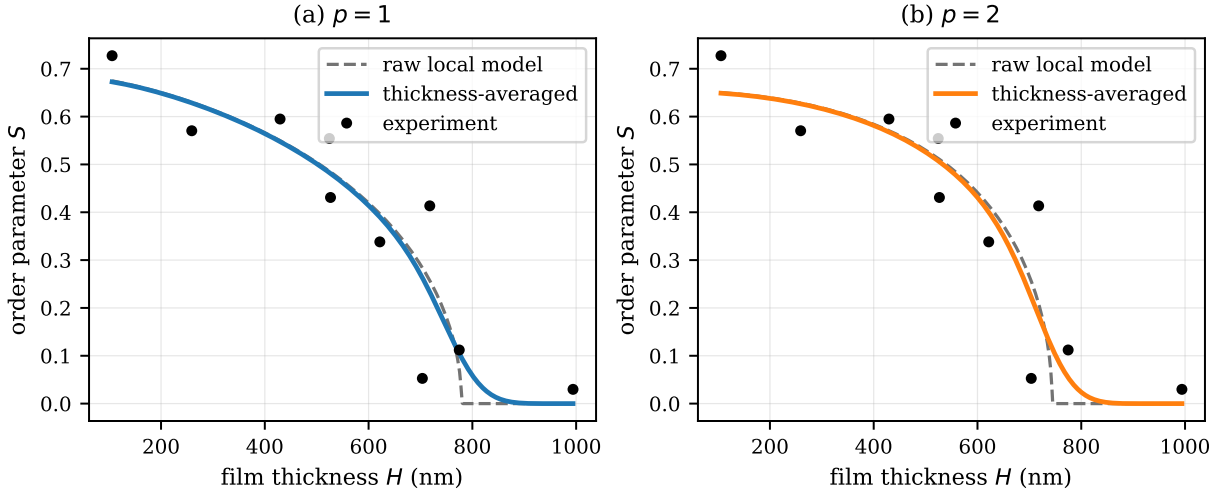


**Figure S4:** Local model $S_0(h)$ (grey dashed) and the thickness-averaged observable $S_{\text{obs}}(H)$ (colored solid) for the (a) $p = 1$ and (b) $p = 2$ kernels, with the experimental data (black circles). Averaging over local wall-thickness variation affects the prediction essentially only near the orientational transition.

## S1.3 Parameter estimation

### S1.3.1 Fitting

The two free parameters, $c_\infty$ and $L$, were determined separately for each kernel by minimizing

$$\mathrm{SSE} = \sum_{i=1}^{10} [S_{\mathrm{obs}}(H_i) - S_i^{\mathrm{exp}}]^2 \tag{S23}$$

over $\log_{10} c_\infty$ and $\log_{10} L$, using differential evolution from multiple independent seeds followed by a local polish. The fibril diameter was fixed at $D = 15$ nm and the thickness variation at $\sigma_H = 50$ nm. The best fits are $c_\infty = 5.98$, $L = 1.24$ $\mu$m, $R^2 = 0.825$ for $p = 1$, and $c_\infty = 5.38$, $L = 0.80$ $\mu$m, $R^2 = 0.812$ for $p = 2$.

### S1.3.2 Sensitivity to the fixed inputs

The fibril diameter $D$ and the thickness variation $\sigma_H$ are fixed rather than fitted. Both were varied over a plausible range and the model refitted from scratch at each value. Because each refit starts afresh, the values at the production inputs differ slightly from the best fits above, within the low-residual valley described in Sec. S1.3.3.

For $p = 1$ the fitted parameters are stable: across a six-fold variation in $D$ (5 to 30 nm) the fitted length changes by less than 2% ($L = 1227$–$1246$ nm) and $R^2$ by less than $10^{-3}$ (Table S2, Fig. S5). The $p = 2$ kernel is stable for $D \geq 10$ nm but moves to a short-length, strong-interaction solution at $D = 5$ nm. The inferred confinement mechanism is therefore insensitive to the value assumed for the fibril diameter, more so for $p = 1$.

The dependence on $\sigma_H$ is also weaker for $p = 1$ than for $p = 2$ (Table S3, Fig. S6). For $\sigma_H \leq 30$ nm the $p = 1$ fit is stable to within 3% in $L$, whereas the $p = 2$ fit switches between two solutions between $\sigma_H = 10$ and 20 nm and alternates between them across the range. At $\sigma_H = 40$ nm the $p = 1$ refit also moves to a short-length solution with clearly degraded fit quality ($R^2 = 0.669$), bracketed by stable fits on both sides. As Sec. S1.3.3 shows, these jumps do not correspond to physically distinct regimes but to the optimiser settling at different points along a single, strongly correlated low-residual valley. The greater stability of the $p = 1$ fit is one of the reasons it is used as the primary kernel.

**Table S2:** Sensitivity of the fitted parameters to the assumed fibril diameter $D$. The production value is $D = 15$ nm.

| $p$ | $D$ (nm) | $c_\infty$ | $L$ (nm) | SSE | $R^2$ |
|---|---|---|---|---|---|
| 1 | 5 | 5.999 | 1245.5 | 0.09455 | 0.8250 |
| 1 | 10 | 5.991 | 1241.8 | 0.09461 | 0.8249 |
| 1 | 15 | 5.983 | 1238.1 | 0.09468 | 0.8248 |
| 1 | 20 | 5.976 | 1234.3 | 0.09475 | 0.8246 |
| 1 | 30 | 5.960 | 1226.7 | 0.09491 | 0.8244 |
| 2 | 5 | 7.720 | 390.1 | 0.12858 | 0.7620 |
| 2 | 10 | 5.321 | 821.6 | 0.10222 | 0.8108 |
| 2 | 15 | 5.403 | 796.6 | 0.10192 | 0.8114 |
| 2 | 20 | 5.375 | 797.4 | 0.10194 | 0.8113 |
| 2 | 30 | 5.248 | 817.9 | 0.10372 | 0.8080 |

**Table S3:** Sensitivity of the fitted parameters to the local wall-thickness heterogeneity $\sigma_H$, from 0 to 100 nm for both kernels to bracket the production value $\sigma_H = 50$ nm (marked).

| $p$ | $\sigma_H$ (nm) | $c_\infty$ | $L$ (nm) | SSE | $R^2$ |
|---|---|---|---|---|---|
| 1 | 0 | 5.925 | 1279.1 | 0.09870 | 0.8173 |
| 1 | 10 | 5.920 | 1284.8 | 0.09902 | 0.8167 |
| 1 | 20 | 5.940 | 1266.7 | 0.09867 | 0.8174 |
| 1 | 30 | 5.956 | 1254.0 | 0.09832 | 0.8180 |
| 1 | 40 | 10.965 | 289.7 | 0.17867 | 0.6693 |
| 1 | **50 (production)** | **5.983** | **1238.1** | **0.09468** | **0.8248** |
| 1 | 60 | 5.991 | 1234.5 | 0.09507 | 0.8240 |
| 1 | 70 | 6.123 | 1135.4 | 0.09157 | 0.8305 |
| 1 | 80 | 6.102 | 1157.9 | 0.08984 | 0.8337 |
| 1 | 90 | 6.084 | 1175.7 | 0.08903 | 0.8352 |
| 1 | 100 | 6.109 | 1164.2 | 0.08834 | 0.8365 |
| 2 | 0 | 7.660 | 393.3 | 0.13186 | 0.7560 |
| 2 | 10 | 7.665 | 392.6 | 0.13180 | 0.7561 |
| 2 | 20 | 5.198 | 875.6 | 0.11299 | 0.7909 |
| 2 | 30 | 5.154 | 895.0 | 0.11148 | 0.7937 |
| 2 | 40 | 5.222 | 867.6 | 0.10566 | 0.8045 |
| 2 | **50 (production)** | **5.345** | **810.0** | **0.10196** | **0.8113** |
| 2 | 60 | 7.651 | 394.7 | 0.12859 | 0.7620 |
| 2 | 70 | 5.341 | 824.8 | 0.09558 | 0.8231 |
| 2 | 80 | 5.393 | 801.1 | 0.09383 | 0.8263 |
| 2 | 90 | 5.384 | 812.0 | 0.09279 | 0.8283 |
| 2 | 100 | 7.553 | 412.0 | 0.12160 | 0.7750 |

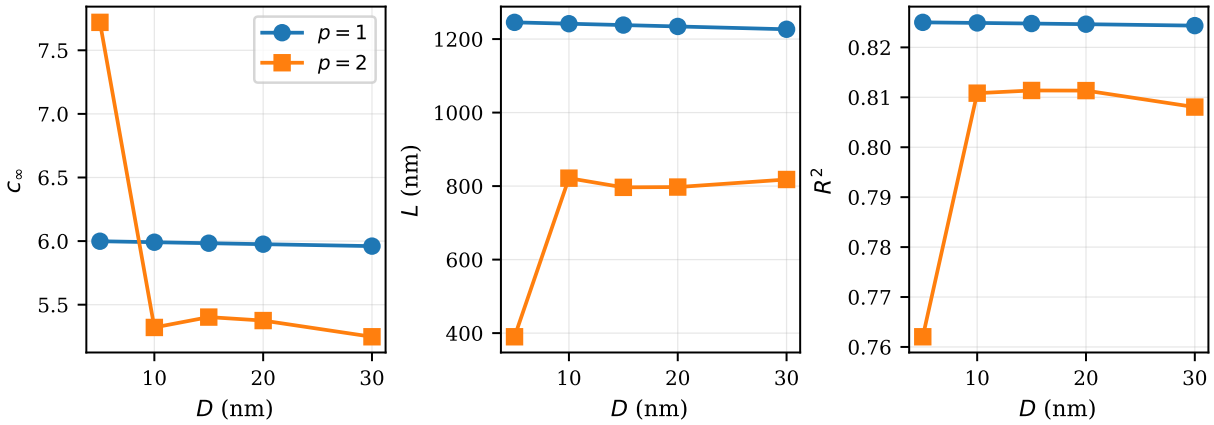


**Figure S5:** Refitted interaction strength $c_\infty$, fibril length $L$ and coefficient of determination $R^2$ as a function of the assumed fibril diameter $D$. The $p = 1$ kernel is essentially independent of $D$ over the whole range.

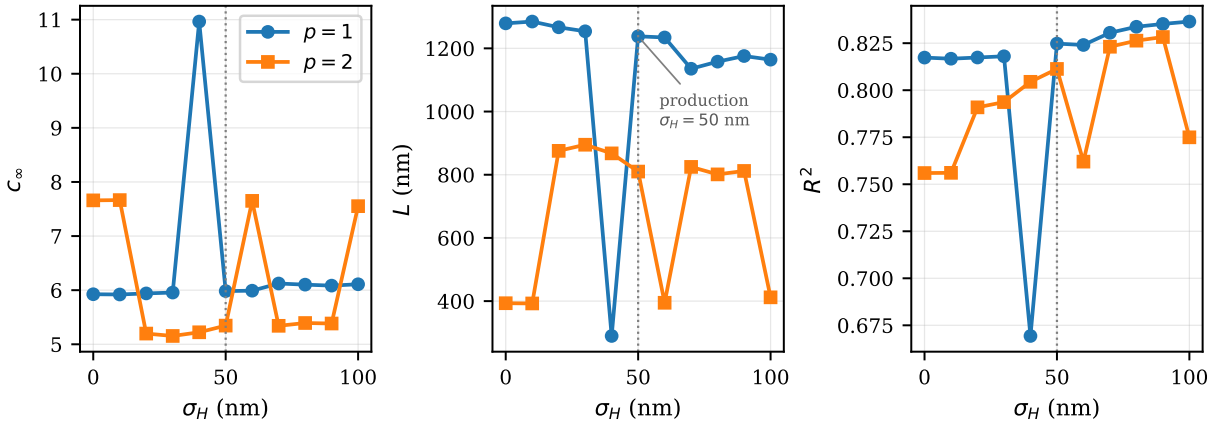


**Figure S6:** Refitted parameters as a function of the assumed local thickness variation $\sigma_H$. The apparent discontinuities reflect the optimizer moving along the correlated $c_\infty$–$L$ valley of Fig. S7, not a change of physical regime.

### S1.3.3 Parameter identifiability

Figure S7 maps the SSE over the $(c_\infty, L)$ plane. For both kernels the low-residual region is not an isolated basin but an elongated, curved valley: an increase in interaction strength can be compensated almost exactly by a decrease in fibril length. The two parameters are therefore strongly correlated; the correlation coefficient between $\log c_\infty$ and $\log L$ across the converged bootstrap resamples of Sec. S1.3.4 is $-0.97$ for $p = 1$ and $-0.98$ for $p = 2$.

This degeneracy is a property of fitting two parameters to a single monotonic crossover measured at ten thicknesses. It does not affect the predicted $S(H)$ curve, which is well constrained along the whole valley, nor the conclusion that confinement drives the loss of order. The fitted $L$ should accordingly be read as the characteristic confinement-relevant contour length implied by a given interaction strength, rather than as an independently determined fibril length; for this reason it was compared with fibril lengths measured directly from SEM images (Sec. S3).

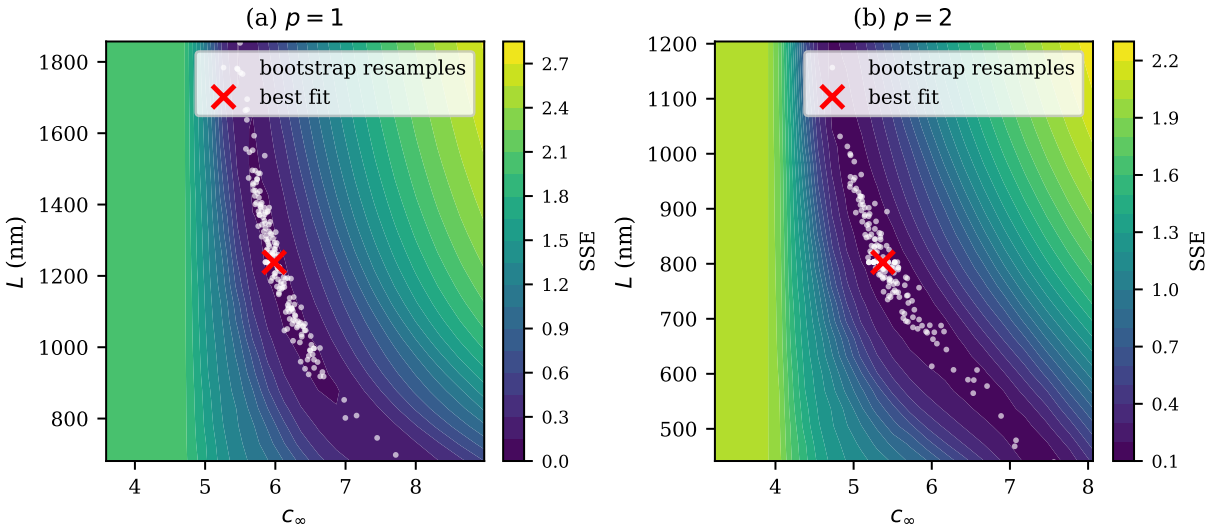


**Figure S7:** SSE over the $(c_\infty, L)$ plane for the (a) $p = 1$ and (b) $p = 2$ kernels, with the best fit (red cross) and the converged bootstrap resamples (white points). The low-residual region forms a single continuous valley along which $c_\infty$ and $L$ trade off; the bootstrap ensemble traces this valley, so the spread of fitted parameters reflects this degeneracy rather than multiple competing solutions.

### S1.3.4 Parameter uncertainty

Confidence intervals were estimated by residual bootstrap. Residuals of the best fit were centred, resampled with replacement and added back to the fitted curve, and the model was refitted locally from the best-fit parameters; 200 resamples were generated for each kernel. A small fraction of resamples failed to converge, collapsing onto the boundary of the search domain with $c_\infty \to 0.1$ and $L$ pinned at its upper limit of 3000 nm. These failures are well separated from the converged fits: every failed resample has $R^2 \leq 0.04$ (most are negative), whereas every retained resample has $R^2 \geq 0.59$. Resamples with $R^2 < 0.5$ were therefore excluded, removing 11 of 200 (5.5%) for $p = 1$ and 8 of 200 (4.0%) for $p = 2$ (Fig. S8).

Excluding the failed refits changes the medians negligibly but tightens the lower bound of the $c_\infty$ interval substantially, from 0.41 to 5.52 for $p = 1$ (Table S4); the unfiltered interval is dominated by the boundary-pinned failures and does not represent genuine parameter uncertainty. From the converged resamples, $c_\infty = 5.99\,[5.52, 7.05]$ and $L = 1238\,[806, 1767]$ nm for $p = 1$, and $c_\infty = 5.38\,[4.96, 7.62]$ and $L = 803\,[383, 967]$ nm for $p = 2$. Because of the correlation described in Sec. S1.3.3, these marginal intervals should not be treated as independent.

**Table S4:** Residual-bootstrap medians and 95% percentile intervals, before and after excluding non-converged resamples. The unfiltered intervals are given for completeness; the converged intervals are those quoted in the main text.

| $p$ | resamples | $c_\infty$ median | $c_\infty$ 95% CI | $L$ median (nm) | $L$ 95% CI (nm) |
|---|---|---|---|---|---|
| 1 | all (200) | 5.97 | [0.41, 7.00] | 1238 | [764, 1875] |
| 1 | converged (189) | 5.99 | [5.52, 7.05] | 1238 | [806, 1767] |
| 2 | all (200) | 5.38 | [0.51, 7.62] | 803 | [383, 1782] |
| 2 | converged (192) | 5.38 | [4.96, 7.62] | 803 | [383, 967] |

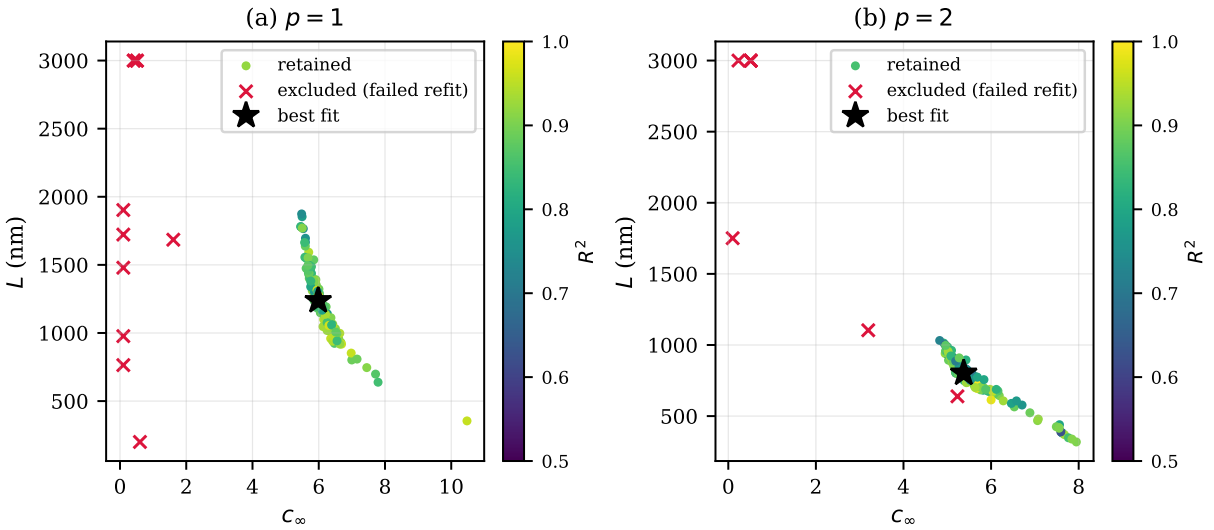


**Figure S8:** Bootstrap parameter ensembles for the (a) $p = 1$ and (b) $p = 2$ kernels. Retained resamples are colored by their coefficient of determination; the resamples excluded as non-converged (red crosses) collapse onto the boundary of the search domain and are clearly separated in fit quality from the retained ensemble. The black star marks the best fit.

### S1.3.5 Residuals

Table S5 and Fig. S9 list the fit residuals at each measured thickness. Away from the transition the model reproduces the data closely, with $|S_{\mathrm{exp}} - S_{\mathrm{model}}| \leq 0.08$ at eight of the ten thicknesses for both kernels. The two largest residuals occur at the two thicknesses closest to the transition, $H = 703.6$ nm ($-0.21$ for $p = 1$) and $H = 717.9$ nm ($+0.18$ for $p = 1$), where two nominally similar films differ in measured order parameter by 0.36. This is where the largest scatter is expected: near the transition $\mathrm{d}S/\mathrm{d}H$ is steepest, so a given local thickness variation or sample-to-sample difference in the imaged region translates into the largest spread in $S$. The two outlying points bracket the model curve rather than lying on one side of it, and no comparable structure appears elsewhere in the residuals.

**Table S5:** Measured and predicted order parameters with residuals for both interaction kernels.

| $H$ (nm) | $S_{\mathrm{exp}}$ | $S_{\mathrm{pred}}$ ($p = 1$) | residual ($p = 1$) | $S_{\mathrm{pred}}$ ($p = 2$) | residual ($p = 2$) |
|---|---|---|---|---|---|
| 105.7 | 0.7273 | 0.6726 | +0.0547 | 0.6489 | +0.0784 |
| 259.2 | 0.5704 | 0.6287 | −0.0583 | 0.6268 | −0.0564 |
| 429.4 | 0.5949 | 0.5478 | +0.0471 | 0.5678 | +0.0271 |
| 524.4 | 0.5542 | 0.4829 | +0.0713 | 0.5074 | +0.0468 |
| 526.6 | 0.4309 | 0.4812 | −0.0503 | 0.5057 | −0.0748 |
| 621.7 | 0.3381 | 0.3902 | −0.0521 | 0.4005 | −0.0624 |
| 703.6 | 0.0527 | 0.2602 | −0.2075 | 0.2088 | −0.1561 |
| 717.9 | 0.4134 | 0.2351 | +0.1783 | 0.1848 | +0.2286 |
| 774.7 | 0.1121 | 0.1075 | +0.0046 | 0.0614 | +0.0507 |
| 994.0 | 0.0298 | 0.0000 | +0.0298 | 0.0000 | +0.0298 |

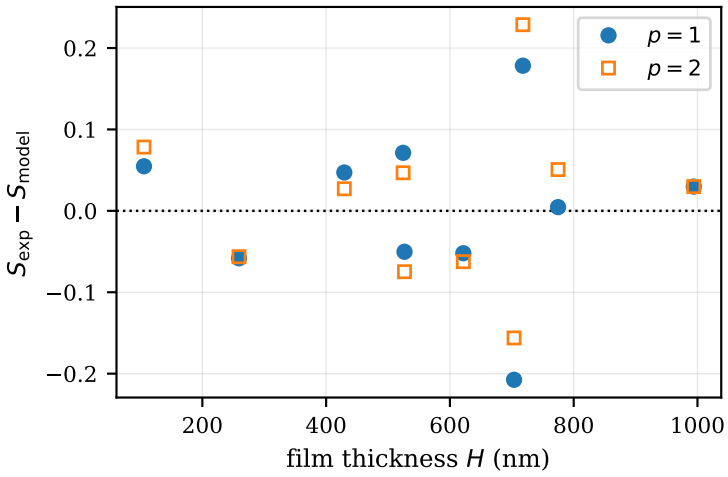


**Figure S9:** Fit residuals $S_{\mathrm{exp}} - S_{\mathrm{model}}$ against film thickness for both kernels. The two largest deviations occur at the two thicknesses closest to the orientational transition, where the predicted order parameter is most sensitive to local thickness variation.

## S2 Freeze-dried foams

To test whether alignment also occurs when the walls form without evaporative drying, MC foams were prepared by freeze-drying. A 1.5 wt% MC solution, prepared as described in the main text, was thermally gelled at 60 °C in plastic containers, frozen for 24 h at −20°C and freeze-dried for 7 days using a Labconco Freezone 2.5 L. The dried foams were fractured, coated and imaged as the other samples.

SEM images of the freeze-dried foams (Fig. S10) show thin walls in which the nanofibrils are aligned in the wall plane, as in the heat-dried foam films. Unlike the heat-dried films, which show small voids between fibrils, the freeze-dried walls show almost no voids between fibrils. Alignment within thin walls is thus not specific to evaporative drying.

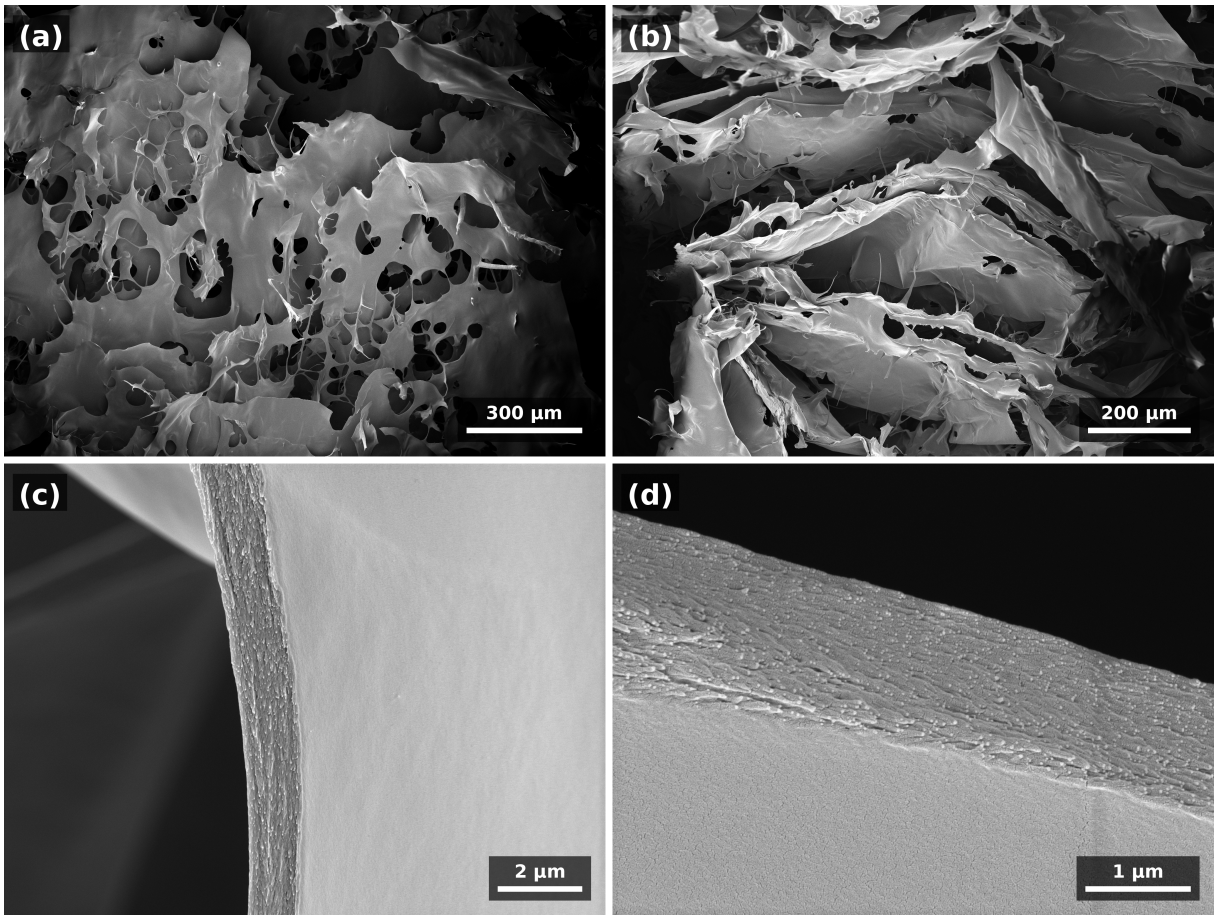


**Figure S10:** SEM images of a freeze-dried MC foam. (a, b) Overall cellular microstructure (75× and 100×). (c) Fractured edge of a cell wall (8.22 k×), showing nanofibril bundles aligned along the wall plane. (d) Fracture surface of a wall at higher magnification (20.5 k×), showing elongated, in-plane-aligned fibrillar features. InLens detector, 2–3 kV.

## S3 Fibril length measurement

The fitted fibril length $L$ was tested against fibril lengths measured directly from SEM images by automated skeleton tracing; the method is described in the main text (Methods). Traced lengths are biased in two opposite ways. Where fibrils overlap and cross, one fibril is broken into several shorter segments, so traced lengths are generally lower bounds on the fibril length and their mean reflects the spacing of crossings rather than the fibril length. Where fibrils are highly aligned, fibrils lying end to end can merge into a single, longer trace. The comparison with $L$ therefore uses the longest traced segments of each image rather than the mean.

Eight images of foam films were analyzed, giving 2821 retained segments (untruncated, straightness $\geq 0.7$, length $\geq 50$ nm). In images 1 and 3–8, the longest segments were 0.55–1.15 $\mu$m long, and the length distributions fell off steeply above this range (Table S6, Fig. S11). Image 2 shows a highly aligned film surface on which segments of up to 2.5 $\mu$m were traced along surface grooves; given the merging of aligned fibrils, these lengths are upper estimates. Representative tracing overlays are shown in Fig. S12.

The sensitivity of the result to the tracing parameters was tested by varying the threshold by $\pm 20\%$ and the spur-pruning length between 20 and 80 nm. Across these settings the pooled 99th percentile of traced lengths ranged from 0.54 to 0.88 $\mu$m (0.72 $\mu$m at default settings), and at most six segments exceeded the fitted length for $p = 1$ in any setting (Table S7).

**Table S6:** Traced segment lengths per image (untruncated segments with straightness $\geq 0.7$).

| Image | segments | longest ($\mu$m) | median of 10 longest ($\mu$m) | 99th percentile ($\mu$m) |
|---|---|---|---|---|
| 1 | 1491 | 0.658 | 0.531 | 0.403 |
| 2 | 275 | 2.491 | 1.276 | 1.529 |
| 3 | 209 | 0.672 | 0.543 | 0.586 |
| 4 | 147 | 0.551 | 0.367 | 0.431 |
| 5 | 133 | 0.759 | 0.373 | 0.561 |
| 6 | 268 | 1.151 | 0.515 | 0.600 |
| 7 | 133 | 0.687 | 0.507 | 0.611 |
| 8 | 165 | 0.758 | 0.367 | 0.448 |

**Table S7:** Sensitivity of the pooled traced-length statistics to the tracing threshold (relative to the Otsu value) and the spur-pruning length, for all eight images. The default settings are shown in bold. Segment counts, longest segment, median of the ten longest and the number of segments longer than the fitted length for $p = 1$ refer to all untruncated segments; the 99th percentile refers to untruncated segments with straightness $\geq 0.7$, as used in the main text.

| Threshold factor | Spur (nm) | Untruncated segments | Longest ($\mu$m) | Median of 10 longest ($\mu$m) | 99th percentile ($\mu$m) | Segments $> 1.24$ $\mu$m |
|---|---|---|---|---|---|---|
| 0.8 | 20 | 4236 | 1.85 | 1.00 | 0.55 | 2 |
| 0.8 | 40 | 4017 | 1.75 | 1.01 | 0.60 | 2 |
| 0.8 | 80 | 3147 | 2.05 | 1.15 | 0.70 | 3 |
| 1.0 | 20 | 3218 | 1.85 | 1.24 | 0.67 | 5 |
| **1.0** | **40** | **2979** | **2.49** | **1.29** | **0.73** | **5** |
| 1.0 | 80 | 2203 | 2.42 | 1.36 | 0.87 | 6 |
| 1.2 | 20 | 2237 | 2.14 | 1.10 | 0.69 | 3 |
| 1.2 | 40 | 1998 | 2.14 | 1.09 | 0.76 | 3 |
| 1.2 | 80 | 1440 | 2.14 | 1.16 | 0.90 | 4 |

## Data and code availability

The numerical model, fitting pipeline, verification analyses and the fibril-tracing code are available upon reasonable request.

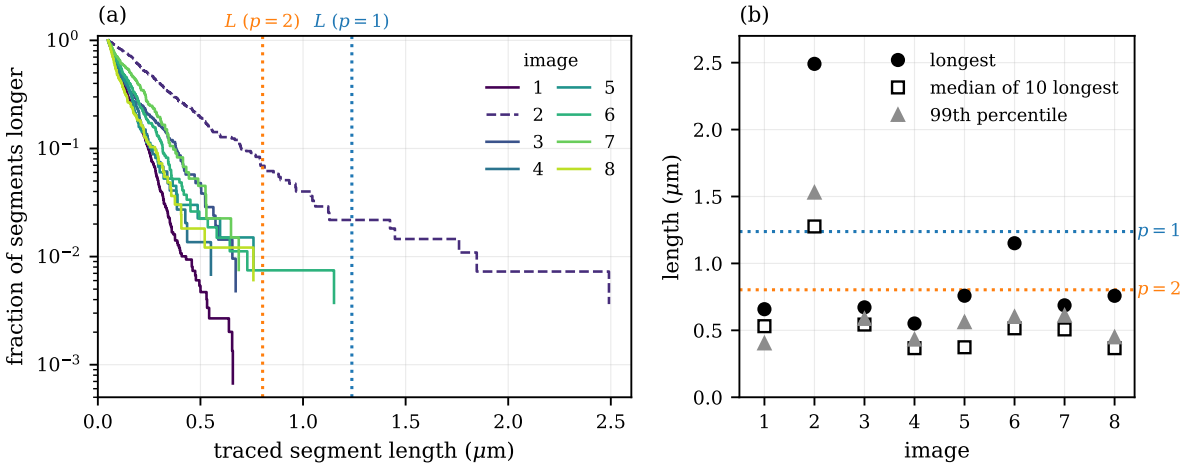


**Figure S11:** Fibril lengths measured by skeleton tracing. (a) Fraction of traced segments longer than a given length for each of eight SEM images of MC foam films (untruncated segments with straightness $\geq 0.7$; 2821 segments in total). Dotted lines mark the fitted effective fibril lengths, $L = 0.80$ $\mu$m ($p = 2$, orange) and $L = 1.24$ $\mu$m ($p = 1$, blue). Because overlapping fibrils break single fibrils into several traced segments, traced lengths are lower bounds on the fibril length. (b) Longest traced segment, median of the ten longest segments, and 99th percentile of traced lengths for each image. In images 1 and 3–8, the longest segments are 0.55–1.15 $\mu$m long. Image 2 shows a highly aligned film surface on which segments of up to 2.5 $\mu$m were traced along surface grooves; since aligned fibrils lying end to end can merge into one trace, these lengths are upper estimates.

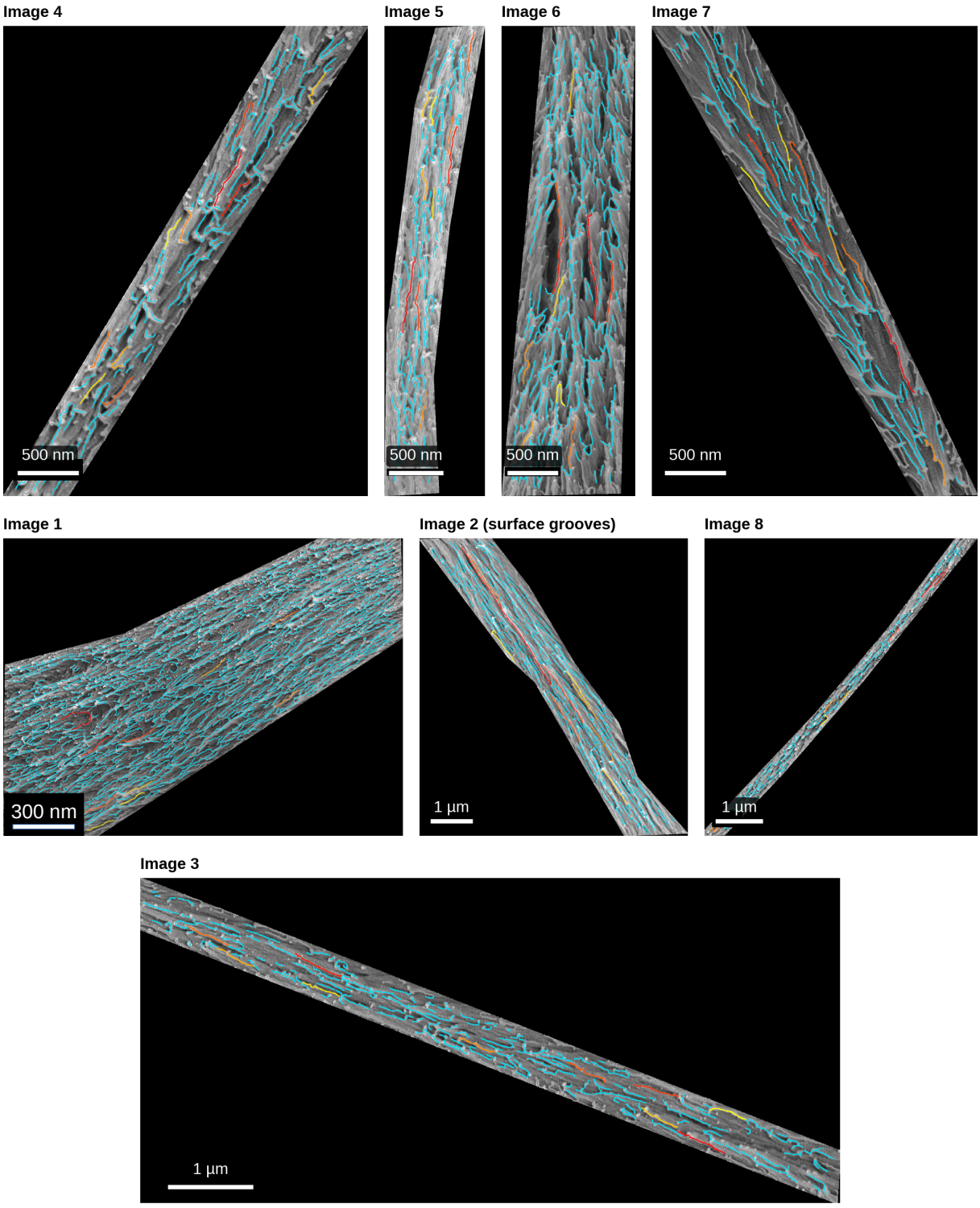


**Figure S12:** Skeleton tracing of all eight SEM images used for the fibril length measurement. Cyan: traced segments; grey: truncated segments (within 50 nm of the region boundary), excluded from the statistics; red to yellow: the ten longest untruncated segments of each image, whose lengths are listed in Table S6. Black regions lie outside the analyzed film area. In image 2, which shows a highly aligned film surface, the longest traces follow surface grooves and may merge fibrils lying end to end; these lengths are therefore upper estimates.